On the Projection of Polarimetric Variables Observed by a Planar Phased-Array Radar at X-Band

William Heberling, *Student Member, IEEE*, and Stephen J. Frasier, *Senior Member, IEEE*

***Abstract*— We present the characteristics of dual-polarized weather radar variables as observed by a planar phased-array radar (PPAR) operating at X-band. The characteristics are governed by the projection of the polarizations radiated by the array into the canonical spherical coordinates defining the measurement geometry of ground-based weather radars. The direction-dependent gain and phase of the radiating elements, the orientation of the radiated polarizations, and the mechanical tilting of the array all contribute to the projection, which results in biased observations compared with those of a mechanically scanned weather radar employing a reflector antenna. We decompose the projection into components that can be separated and customized for various PPAR configurations, including consideration of possible cross-polarized radiation by the elements and the effect of a wet radome covering the array face. These are represented by matrices whose product comprises the total projection. We apply this methodology to an X-band PPAR using in-place measurements of precipitation to obtain the properties of the radiation pattern. We then obtain the resulting biases of common weather radar polarimetric variables. We show that the biases can be represented as a product of the intrinsic variables with projection- and target-dependent corrections. The projection-dependent corrections depend only upon elements of the projection matrix, while the target-dependent corrections also depend upon the intrinsic differential reflectivity and copolar or cross-polar correlation coefficients. We find that the projection-dependent corrections are sufficient to achieve acceptable bias over most of the scan range.**

***Index Terms*— Meteorological radar, phased arrays, radar measurements.**

I. Introduction

While phased-array technology has been available for many years, its application in meteorology is in its infancy. The promise of this technology is being tested and evaluated through fixed radar testbeds, such as the National Weather Radar Testbed (NWRT) [1], [2], the current Advanced Technology Demonstrator [3], [4], mobile Doppler radars for rapid scanning [5]–[7], and low-cost, low-power polarimetric phased-arrays [8]–[11]. Phased-array weather radars allow for more rapid and arbitrary scanning and potentially faster update times (high temporal resolution of severe weather). This is possible due to electronic scanning in which the beam can move nearly instantaneously to any scan direction. In addition, multiple-target or simultaneous-beam scanning becomes possible. Phased-arrays also eliminate moving parts from the system, potentially reducing routine maintenance.

To be viable for meteorological applications, a phased-array antenna must meet certain requirements. The most critical is the ability to make high-fidelity dual-polarization measurements that are necessary for accurate rainfall estimates, hydrometeor classification, and morphological analysis of storm structure. As a result, operational weather radars require rigorous initial and periodic calibration. Performing such calibration with a phased array is significantly more complex than for a reflector antenna due to the varying beam gain, beam shape, and polarization properties with the scan angle. New techniques must be developed and tested to ensure that the data quality is not degraded by the introduction of phased-array radars.

It has been shown that dual-polarized phased arrays exhibit particular polarization properties that can give rise to biases in common weather radar observables. These biases are particularly prevalent when the array scans away from the principal planes of the antenna, and they may be significant enough to exceed the tolerances required by meteorological applications. Zhang *et al.* [12] presented the polarimetric bias in terms of the projection of the radiated fields by a planar phased-array radar (PPAR) to the far-field assuming crossed dipole radiators, and Zrnic *et al.* [13] considered this same projection combined with Doppler shift. Doviak *et al.* [14] compared the measurements of cross-polar radiation from a PPAR with theory. Lei *et al.* [15] considered the projection from waveguide aperture and microstrip patch radiators that are represented as equivalent magnetic dipole radiators. In [16], they also compared theoretical biases between reflector antennas and both planar and cylindrical arrays. Pang *et al.* [17] considered measurement errors of individual element patterns on polarimetric biases. Limited investigations of polarimetric bias were conducted in the field by Orzel and Frasier [18] who used a dual-polarized phased-array capable of electronic scanning on 1-D only. Most recently, Li *et al.* [19] have evaluated the quality of polarimetric measurements from an S-band PPAR.

In this article, we describe the projection and polarimetric bias properties of an X-band dual-polarization radar operated by the Microwave Remote Sensing Laboratory (MIRSL) of the

Manuscript received April 28, 2020; revised August 5, 2020; accepted September 5, 2020. Date of publication September 24, 2020; date of current version April 22, 2021. This work was supported by the National Science Foundation, University of Massachusetts, under Grant AGS-1655693. *(Corresponding author: Stephen J. Frasier.)*

The authors are with Microwave Remote Sensing Laboratory, University of Massachusetts at Amherst, Amherst, MA 01003 USA (e-mail: wheberling@umass.edu; frasier@umass.edu).

Color versions of one or more of the figures in this article are available online at https://ieeexplore.ieee.org.

Digital Object Identifier 10.1109/TGRS.2020.3023640

University of Massachusetts. The radar system is a prototype of the "Skyler" radar system [11] developed by Raytheon and made available to MIRSL for research purposes. Section II begins by briefly summarizing the projection methodology of previous investigators. We then decompose the projection problem into terms associated with: 1) the radiating elements' amplitude and phase patterns; 2) their equivalent sources that dictate the orientation of radiated fields; and 3) their orientation in space. We show how crossed-polarized radiation from imperfect radiators can also be incorporated. This decomposition is useful because it allows us to first characterize the antenna in its native polarization basis using observations of light precipitation. Such an approach could be used to perform periodic polarimetric calibration. We present expressions for the projected polarimetric variables with two levels of correction: one dependent upon the projection only, and another also dependent upon the intrinsic properties of the scattering. Henceforth, we will refer to these as projection-dependent corrections and target-dependent corrections.

In Section III, we briefly describe the Skyler prototype system and its deployment to estimate its amplitude and phase patterns from field measurements. We incorporate these measurements with the deployment parameters to obtain the full projection matrix. We then evaluate the biases in polarimetric products and their correction.

II. Projection of Fields by a PPAR

A. Methodology

The projection of fields radiated by elements of a planar phased-array follows the descriptions provided by Zhang *et al.* [12] and subsequent works [13], [15], [16]. These works express the relationship between the fields at the radiating aperture and the far-field through a so-called projection matrix. This projection occurs upon transmission and again upon reception of the radar echo. Beyond the radiating aperture, the propagation and backscattering characteristics of the radar signal are described by the same intrinsic scattering parameters as are present with radars employing conventional reflector antennas. The resulting projected scattering parameters are related to their intrinsic counterparts through

$$\mathbf{S}^{(\mathbf{p})} = \mathbf{P}^{T}\mathbf{S}\,\mathbf{P} \tag{1}$$

where $\mathbf{S}^{(\mathbf{p})}$ is the scattering matrix (including propagation effects) that would be measured by a PPAR, $\mathbf{S}$ is the intrinsic scattering matrix (also including propagation effects) that would be measured by a mechanically scanned radar, and $\mathbf{P}$ is the matrix that projects the radiated field at the array face, E_t, into the incident fields at the scattering location in the far-field, E_i

$$E_i = \begin{matrix} E_{i\varphi} \\ -E_{i\theta} \end{matrix} = \mathbf{P} \begin{matrix} E_{th} \\ E_{tv} \end{matrix} = \mathbf{P}E_t \tag{2}$$

and where

$$\mathbf{P} = \begin{matrix} p_{11} & p_{12} \\ p_{21} & p_{22} \end{matrix} = \begin{matrix} E_{\varphi}^{(h)} & E_{\varphi}^{(v)} \\ -E_{\theta}^{(h)} & -E_{\theta}^{(v)} \end{matrix}. \tag{3}$$

The superscripts (h) and (V) denote the polarization of the wave excited at the element. In (1), $\mathbf{P}^{\mathbf{T}}$ is the transpose matrix

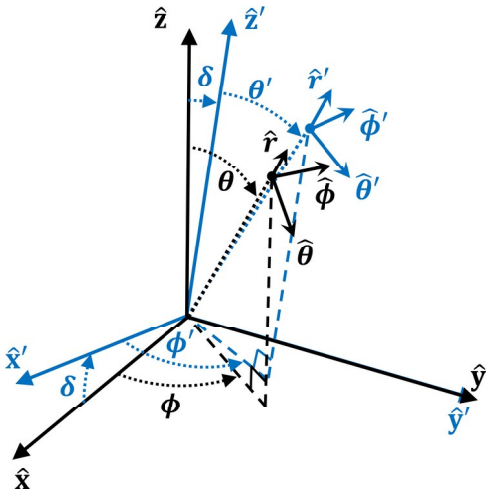

Fig. 1. Coordinate system. World-relative coordinates and unit vectors are unprimed, array-relative coordinates, and unit vectors are primed. The array face lies in the y'–z' plane centered at the origin.

that projects the far-field back to the PPAR upon reception. Lei *et al.* [15] showed that, for microstrip patch radiators, the projection matrix is given by

$$\mathbf{P} = \begin{matrix} \sin\theta \cdot g^{(h)}(\theta\,,\,\varphi) & \cos\theta\sin\varphi \cdot g^{(v)}(\theta\,,\,\varphi) \\ 0 & \cos\varphi \cdot g^{(v)}(\theta\,,\,\varphi) \end{matrix} \tag{4}$$

where it was assumed that the array face lay in the yz plane and the broadside direction was along the x-axis (see Fig. 1). Here, $g^{(h,v)}$ represents the element's radiated electric field pattern (less a dipole term).

Then, they demonstrate a theoretical correction for radiators in both alternate transmit/simultaneous receive (ATSR) and simultaneous transmit/simultaneous receive (STSR) modes. They showed that $\mathbf{S}$ could, in principle, be retrieved from $\mathbf{S}^{(\mathbf{p})}$ by means of a correction matrix $\mathbf{C}$

$$\mathbf{S} = \mathbf{C}^{\mathbf{T}}\mathbf{S}^{(\mathbf{p})}\mathbf{C} \tag{5}$$

where $\mathbf{C} = \mathbf{P}^{-1}$. They also present a set of equations relating intrinsic second moment weather products to the corresponding measured weather products using the projection matrix. In general, the projected polarimetric products depend upon the intrinsic products, elements of $\mathbf{P}$, and upon the differential reflectivity Z_{dr}, and the copolar correlation coefficient's (ρ_{hv}) magnitude and phase.

B. Projection Components

We now reproduce the above projection methodology expressed in terms that are more easily separated. To do so, a precise definition of coordinate systems and cross-polarization is necessary. Aboserwal *et al.* [20] have approached this issue, describing in detail the polarization definitions famously set forth by Ludwig [21] and the implications of their use for weather radar. For weather radar applications by a PPAR, none of Ludwig's definitions are exactly appropriate, and instead, a coordinate system based on the weather scatterers' frame of reference (gravity, the ground) should be used.

Following prior works, we begin with the z-axis parallel to gravity (vertical) and the x-axis parallel to antenna broadside direction with the planar array located in the yz plane, as indicated in Fig. 1. In the far-field, spherical coordinates are used, where the world-relative horizontal polarization is aligned with $\hat{\varphi}$ and the "vertical" polarization is aligned with $-\hat{\theta}$. In addition, it is useful to define a tilted array coordinate system because phased array antennas are often operated with the planar array tilted upward in elevation. Thus, for some tilt angle δ, a new coordinate basis is formed using primed coordinates x', y', z', φ', and θ'.

We express the projection matrix as the product of three sources contributing to polarization bias. Each of these sources is itself represented by a matrix. The sources are as follows.

1) *Main Beam Gain and Relative Phase* **G**: This is simply the amplitude and phase pattern of the radiating elements with the scan angle. It is expressed in terms of the native polarizations radiated by the elements of the PPAR.
2) *Radiated Dipole Polarizations* **D**: This considers the effect of the radiated polarization of the dual-polarized elements with scan angle, and it relates the native polarization of the elements to the array-relative azimuth and elevation directions (φ, θ). Element polarizations are expressed in terms of equivalent electric dipoles or magnetic dipoles depending upon the nature of the element.
3) *Array Tilt and Roll Projection* **T**: Finally, the PPAR antenna is often tilted. The abovementioned effects are all associated with the array-relative scan angle, but the intrinsic scattering must be related to world-relative coordinates.

With this framework, the final projection matrix is given by

$$\mathbf{P} = \mathbf{TDG} \tag{6}$$

where the subsequent left-multiplied matrices may be viewed as occurring in sequence during transmission. In the following, we describe the individual terms.

C. Main Beam Gain and Relative Phase

First, the calibration of the array itself must be included. The radiating elements and associated electronics introduce an array-relative, scan angle-dependent amplitude and phase. These are analogous to the $g^{(h,v)}$ terms described in [15], though not identical as will be seen shortly. In practice, this needs to be calibrated via laboratory or field measurements and poses the greatest challenge. The results can then be represented as the amplitude and phase correction for both H and V channels at each scan angle. For an array consisting of ideal dual-polarized radiators

$$\mathbf{G} = \begin{matrix} g_{hh}(\theta, \varphi) & 0 \\ 0 & g_{vv}(\theta, \varphi)e^{j\beta(\theta,\varphi)} \end{matrix} \tag{7}$$

where g_{hh} and g_{vv} are the one-way voltage gains for the horizontal and vertical channels, respectively, and β is the system differential phase between the H and V channels, all of which are a function of array-relative scan angle (θ, φ). For simplicity, we consider no cross-polarized radiation from the elements ($g_{hv} = g_{vh} = 0$). The case of cross-polarized radiation can be handled and is discussed later.

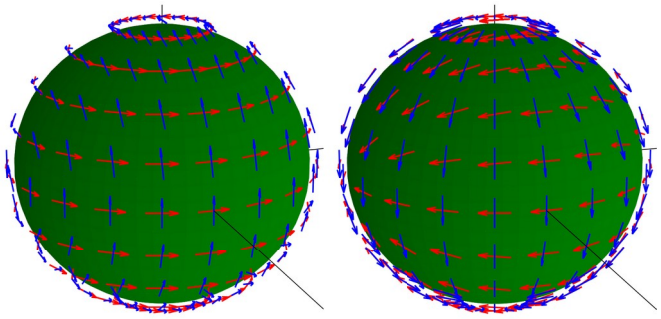

Fig. 2. Depiction of radiated electric field polarization vectors with scan angle for (Left) magnetic dipole radiators and (Right) electric dipole radiators. The horizontal polarization is indicated in red, while the vertical polarization is indicated in blue.

At this point, it should also be mentioned that, if **G** is determined through field observations (as is done in Section IV), it is likely that the radome covering the array face may be wet. If the radome is a planar radome attached to the array face, as in our case, then the presence of water can yield a direction-dependent attenuation and excess phase. In principle, this can be incorporated into **G**. We discuss the treatment of a planar wet radome in the Appendix. If the array lies inside a spherical radome, then the treatment is identical to that for reflector antennas.

D. Radiated Dipole Polarizations

While the **G** matrix accounts for spatially varying amplitudes and phases introduced by array elements, it does not consider the orientation of their radiated fields. This is the purpose of the dipole matrix (**D**). It projects the H and V channel voltages into their respective $\hat{\varphi}$ and $\hat{\theta}$ vector components, where $\hat{\varphi}$ and $\hat{\theta}$ are the array-relative spherical coordinates, as indicated in Fig. 1. For practical radiators, the "horizontal" and "vertical" polarized fields become nonorthogonal when electronically scanning off the principal planes, introducing coupling between the polarizations. For a microstrip patch or waveguide aperture element, the equivalent sources are magnetic currents, whereas, for crossed dipole elements, the equivalent sources are electric currents. Fig. 2 illustrates the orientation of electric fields as a function of radiation direction for both horizontally polarized and vertically polarized electric current sources and magnetic current sources. In general, the **D** matrix is expressed as

$$\mathbf{D} = \begin{matrix} \hat{u}^{(h)} \cdot \hat{\varphi} & \hat{u}^{(v)} \cdot \hat{\varphi} \\ \hat{u}^{(h)} \cdot \hat{\theta} & \hat{u}^{(v)} \cdot \hat{\theta} \end{matrix} \tag{8}$$

where the vectors $\hat{u}^{(h,v)}$ are the far-field unit vectors of the fields produced by the equivalent current sources for each polarization. The copolarized and cross-polarized unit vectors for both types of current sources are given in [20, Table III]. The far-field unit vectors for $\hat{z}$- and $\hat{y}$-oriented magnetic current sources (corresponding to H-polarized and V-polarized

microstrip patch antennas, respectively) are

$$\hat{u}^{(h)} = \hat{\varphi} \tag{9}$$

$$\hat{u}^{(v)} = \frac{\cos\theta \sin\varphi \hat{\varphi} - \cos\varphi \hat{\theta}}{\sqrt{1-\sin^2\theta \sin^2\varphi}}. \tag{10}$$

As a result, for magnetic dipole radiators, $\mathbf{D}$ is given by

$$\mathbf{D_m} = \begin{bmatrix} 1 & \frac{\sin\varphi \cos\theta}{\sqrt{1-\sin^2\theta \sin^2\varphi}} \\ 0 & \frac{-\cos\varphi}{\sqrt{1-\sin^2\theta \sin^2\varphi}} \end{bmatrix} \tag{11}$$

while, for electric dipole radiators, $\mathbf{D}$ is given by

$$\mathbf{D_e} = \begin{bmatrix} \frac{-\cos\varphi}{\sqrt{1-\sin^2\theta \sin^2\varphi}} & 0 \\ \frac{-\sin\varphi \cos\theta}{\sqrt{1-\sin^2\theta \sin^2\varphi}} & 1 \end{bmatrix}. \tag{12}$$

The denominators in the abovementioned matrix entries are normalizations for the unit vectors. We see that, for magnetic dipole radiators, the horizontal polarization aligns with the unit vector $\hat{\varphi}$, while the vertical polarization does not align with $\hat{\theta}$. For electric dipole radiators, the vertical polarization aligns with $\hat{\theta}$, while the horizontal polarization does not align with $\hat{\varphi}$. Similar to the discussion in [15], the matrices $\mathbf{D_m}$ and $\mathbf{D_e}$ are related

$$(\mathbf{D_m}^T)^{-1} \propto \mathbf{D_e}$$
$$(\mathbf{D_e}^T)^{-1} \propto \mathbf{D_m}. \tag{13}$$

For a PPAR consisting of microstrip patch radiating elements, the product of $\mathbf{DG}$ is given by

$$\mathbf{DG} = \begin{bmatrix} g_{hh}(\theta, \varphi) & \frac{\sin\varphi \cos\theta}{\sqrt{1-\sin^2\theta \sin^2\varphi}} g_{vv}(\theta, \varphi) \\ 0 & \frac{-\cos\varphi}{\sqrt{1-\sin^2\theta \sin^2\varphi}} g_{vv}(\theta, \varphi) \end{bmatrix} \tag{14}$$

where the system differential phase term associated with g_{vv} has been suppressed for clarity. This is equivalent to the projection matrix described in (4), as described in [12] and [15]; however, there is a notable difference in representation. In (4), the definitions of the horizontally polarized element pattern term $g^{(h)}$ did not include a $\sin\theta$ term representative of a Hertzian dipole radiation pattern, so the far-field pattern was defined as $E_\varphi \approx \sin\theta\, g^{(h)}(\theta, \varphi)$. In (14), the $\sin\theta$ term is incorporated into g_{hh}. Similarly, for the vertically polarized element pattern, the same "$\sin\theta$-like" term is incorporated into g_{vv} and is accounted for in the normalizations of the unit vectors in $\mathbf{D}$. The relationship between the two representations can be written

$$\begin{aligned} g_{hh} &= \sqrt{\sin^2\theta} \cdot g^{(h)} \\ g_{vv} &= \sqrt{\cos^2\theta \sin^2\varphi + \cos^2\varphi} \cdot g^{(v)}. \end{aligned} \tag{15}$$

While this seems like a trivial difference in notation, it is significant. The $\mathbf{G}$ matrix represents the amplitudes and relative phase that are measured, for example, by a PPAR observing a collection of spherical scatterers uniformly distributed over the field of view without any projection. That is, it represents the direct response of the PPAR in its native polarization basis as defined by the radiating elements and, thus, represents the "raw" amplitude and phase measurement of the phased array. This matrix can be obtained through routine measurements of natural targets averaged over space (range) and time, for example, in light precipitation. The remaining components of the projection matrix are determined entirely by geometry.

E. Array Tilt and Roll

The abovementioned results are specific to a PPAR lying in the yz plane with the broadside direction along the x-axis. In this case, the array-relative scan angles, θ and φ, and unit vectors, $\hat{\theta}$ and $\hat{\varphi}$, are equal to the world-relative scan angles, θ and φ, and unit vectors $\hat{\theta}$ and $\hat{\varphi}$. It is common, however, to tilt the array such that the broadside direction points toward the middle of the range of desired elevation coverage, so as to optimize the scan range in elevation. This is a rotation about the y-axis by an angle δ, as shown in Fig. 1. In a mobile operation, it is conceivable that there might be a small roll angle as well (a rotation about the x-axis by an angle γ), so this is also considered here. The coordinate rotation is achieved by converting to Cartesian coordinates (via matrix $\mathbf{T_1}$), performing the rotations ($\mathbf{T_2}$), and then converting to world-relative spherical coordinates ($\mathbf{T_3}$)

$$\begin{bmatrix} \hat{\varphi} \\ \hat{\theta} \end{bmatrix} = \mathbf{T} \begin{bmatrix} \hat{\varphi} \\ \hat{\theta} \end{bmatrix}, \quad \mathbf{T} = \mathbf{T_3}\, \mathbf{T_2}\, \mathbf{T_1} \tag{16a}$$

$$\mathbf{T_1} = \begin{bmatrix} -\sin\varphi & \cos\varphi \cos\theta \\ \cos\varphi & \sin\varphi \cos\theta \end{bmatrix} \tag{16b}$$

$$\mathbf{T_2} = \begin{bmatrix} \cos\delta & 0 & -\sin\delta \\ \sin\gamma \sin\delta & \cos\gamma & \sin\gamma \cos\delta \\ \cos\gamma \sin\delta & -\sin\gamma & \cos\gamma \cos\delta \end{bmatrix} \tag{16c}$$

$$\mathbf{T_3} = \begin{bmatrix} -\sin\varphi & \cos\varphi & 0 \\ \cos\theta\cos\varphi & \cos\theta\sin\varphi & -\sin\theta \end{bmatrix}. \tag{16d}$$

It is also possible to relate the array-relative scan angle (φ, θ) to the world-relative scan angle (φ, θ) using

$$\cos\theta = \sin\theta\cos\varphi \cos\gamma \sin\delta - \sin\theta \sin\varphi \sin\gamma + \cos\theta \cos\gamma \cos\delta \tag{17a}$$

$$\tan\varphi = \frac{\sin\theta\cos\varphi \sin\gamma \sin\delta + \sin\theta \sin\varphi \cos\gamma + \cos\theta \sin\gamma \cos\delta}{\sin\theta\cos\varphi \cos\delta - \cos\theta \sin\delta}. \tag{17b}$$

The final resulting matrix, $\mathbf{P = TDG}$, projects the radiated fields of the tilted PPAR into world-relative coordinates. It is worth noting that, while the radiators exhibit particular alignments with the array-relative unit vectors, $\hat{\theta}$ and $\hat{\varphi}$, once the array is tilted, these unit vectors are no longer aligned with the world-relative $\hat{\theta}$ and $\hat{\varphi}$. Thus, all elements of the final projection matrix are nonzero. The action of this projection on the intrinsic scattering parameters, $\mathbf{S}$, and on the polarimetric second-moment products is the same as that derived in prior works [12], [15] and is discussed shortly.

F. Consideration of Cross-Polarized Radiation

The **G** matrix presented earlier assumed ideal elements producing no cross-polar radiation. Cross-polar radiation from imperfect elements can be treated directly in **G** if it can be assumed that the source of the cross-polar radiation is that from a rotated dipole of the same type as that producing the copolar radiation and not from some other equivalent source. For example, a microstrip patch excited in horizontal polarization is represented by an equivalent z-directed magnetic dipole. Cross-polar radiation from this source that can be represented in **G** would be that due to an equivalent y-directed magnetic dipole. With this assumption, the product **DG** is given by (18), as shown at the bottom of the page.

This representation describes cross-polarization observed at the aperture resulting in cross-polarized far-fields that are not orthogonal to the copolarized fields except along the principal planes. This representation is correct to the extent that the cross-polarized radiation comes from the assumed source. If, instead, the cross-polarized radiation is due to spurious radiation from another source, such as feedlines or other structures on or near the antenna, then the assumed projection may be wrong.

Alternatively, one could consider the cross-polarized radiation in the far-field. Cross-polarization unit vectors can be defined for the horizontal and vertically oriented dipole radiators, and these unit vectors are orthogonal to their copolarized counterparts. However, the equivalent source producing these cross-polarized fields, are of opposite types, as described in [20]. That is, the equivalent source of the cross-polar fields of a z-directed magnetic current source is a z-directed electric current source. This cannot be treated directly in **G** since it must be multiplied by a different **D**. One can, however, treat them separately by putting the off-diagonal terms of **G** in a separate matrix, say $\mathbf{G^x}$, multiplying by an appropriate $\mathbf{D^x}$, and then adding the results. With this approach, the $\mathbf{D^x}$ matrices are defined as in (11) and (12) but of the opposite source type

$$\mathbf{D_m^x} = \mathbf{D_e}, \quad \mathbf{D_e^x} = \mathbf{D_m}. \tag{19}$$

Using this formulation for a microstrip patch radiator, we obtain

$$\mathbf{DG} + \mathbf{D^xG^x} = \begin{bmatrix} g_{hh} & g_{hv}\dfrac{-\cos\varphi}{\sqrt{1-\sin^2\theta\,\sin^2\varphi}} + g_{vv}\dfrac{\sin\varphi\,\cos\theta}{\sqrt{1-\sin^2\theta\,\sin^2\varphi}} \\ g_{vh} & g_{hv}\dfrac{-\sin\varphi\,\cos\theta}{\sqrt{1-\sin^2\theta\,\sin^2\varphi}} + g_{vv}\dfrac{-\cos\varphi}{\sqrt{1-\sin^2\theta\,\sin^2\varphi}} \end{bmatrix} \tag{20}$$

which is seen to be different from the earlier case. While the projections are different, it is important to remember that the definitions of g_{hv} and g_{vh} are also different in the two cases. In the former case, they are defined in terms of orthogonal (but otherwise identical) sources at the aperture; whereas, in the second case, they are defined by orthogonal polarizations in the far-field.

Choosing the appropriate representation depends upon the application and the method of characterizing cross-polar radiation. The former approach more easily represents what might be measured in a near-field chamber. Although the latter approach requires a slight modification to the original equations, it can be easily constructed from the far-field pattern of a single element. To the extent that the latter approach relies upon truly cross-polarized fields at the target location, it seems to be the appropriate definition. That is, field observations of nondepolarizing scatterers with imperfect elements would result in a cross-polar response consistent with the latter definition.

While this treatment has been included here for completeness, we do not consider cross-polarized radiation in our subsequent analysis. The elements used in our case exhibit low cross-polar radiation such that it could not be measured with sufficient signal-to-noise ratio from field measurements.

G. Correction to Polarimetric Variables

The expressions describing the biased observations of the PPAR in terms of intrinsic values and the projection matrix were derived for ATSR mode (also valid for ATAR mode) in [12] and [15]. With some algebraic manipulation, their expressions for reflectivity factor, differential reflectivity, and copolar correlation coefficient can be expressed as follows:

$$Z_h^{(p)} = Z_h\,|p_{11}|^4(1 + Z_h) \tag{21}$$

$$Z_{dr}^{(p)} = Z_{dr}\left(\frac{p_{11}}{p_{22}}\right)^4 \frac{1 + Z_h}{1 + Z_v} \tag{22}$$

$$\rho_{hv}^{(p)} = \rho_{hv}\left(\frac{p_{11}p_{22}^*}{|p_{11}||p_{22}|}\right)^2 \sqrt{\frac{(1+\rho_{hv})}{(1+Z_h)(1+Z_v)}} \tag{23}$$

where (p) superscripts represent projected variables observed by the PPAR, primes denote intrinsic values (that would be observed by a mechanically scanning radar), and p_{ij} are elements of the projection matrix, which may be complex-valued. In each of these expressions, the projected variable is expressed as the product of the intrinsic variable, a projection-dependent term involving diagonal elements of a projection matrix only, and a target-dependent term involving the off-diagonal elements of the projection matrix along with intrinsic variables Z_{dr} and ρ_{hv}. These target-dependent terms are given by

$$Z_h = \frac{|p_{21}|^4 Z_{dr}^{-1} + 2Re\,[\rho_{hv}p_{11}^2 p_{21}^{*2}]Z_{dr}^{-1/2}}{|p_{11}|^4}, \tag{24}$$

$$\mathbf{DG} = \begin{bmatrix} g_{hh} + g_{vh}\dfrac{\sin\varphi\,\cos\theta}{\sqrt{1-\sin^2\theta\,\sin^2\varphi}} & g_{hv} + g_{vv}\dfrac{\sin\varphi\,\cos\theta}{\sqrt{1-\sin^2\theta\,\sin^2\varphi}} \\ g_{vh}\dfrac{-\cos\varphi}{\sqrt{1-\sin^2\theta\,\sin^2\varphi}} & g_{vv}\dfrac{-\cos\varphi}{\sqrt{1-\sin^2\theta\,\sin^2\varphi}} \end{bmatrix} \tag{18}$$

$$Z_V = \frac{|p_{12}|^4 Z_{dr} + 2Re[\rho_{hv} p_{12}^2 p_{22}^{*2}] Z_{dr}^{1/2}}{|p_{22}|^4}, \quad (25)$$

$$\rho_{hv} = \frac{p_{11}^2 p_{12}^{*2} Z_{dr}^{1/2} + p_{12}^{*2} p_{21}^2 \rho_{hv}^* + p_{21}^2 p_{22}^{*2} Z_{dr}^{-1/2}}{p_{11}^2 p_{22}^{*2} \rho_{hv}}. \quad (26)$$

The linear depolarization ratio (LDR) is defined in terms of world-relative horizontal and vertical polarizations. LDR_h is defined as the ratio of vertically polarized power received to horizontally polarized power received when horizontal polarization is transmitted. LDR_v is the ratio of horizontally polarized power received to vertically polarized power received when vertical polarization is transmitted. Either measurement requires that the radar transmit and receive in alternating polarizations, so as to measure both copolarized and cross-polarized echoes. With this same definition, one can define the LDR of a PPAR.

Expressions for LDR_h and LDR_v were presented in [15] in the absence of any cross-polarized scattering. Their expressions indicated only the lower bound on LDR that could be observed given the projection and nonorthogonality of polarizations and were, therefore, independent of the intrinsic LDR. By including the possibility of cross-polarized scattering, the LDR_h observed by a PPAR can be expressed in a manner consistent with the other variables

$$\mathrm{LDR}_h^{(p)} = \mathrm{LDR}_h \frac{|p_{11}p_{22} + p_{12}p_{21}|^2}{|p_{11}|^4} \frac{1 + \mathrm{LDR}_h}{1 + Z_h} + \mathrm{LDR}_{h,\min} \quad (27)$$

where (28) and (29), as shown at the bottom of the page, where ρ_{hx} and ρ_{vx} are the intrinsic cross-polar correlation coefficients. In obtaining these expressions, it has been assumed that $s_{hv} = s_{vh}$ as is the case for reciprocal media. Also, because LDR_h necessarily involves cross-polar measurements, the projection-dependent correction term includes off-diagonal elements of the projection matrix. The expression for $\mathrm{LDR}_h^{(p)}$ differs from the other variables in which there is also an additive term. The term $\mathrm{LDR}_{h,\min}$ is the same term as was derived by [15]. Namely, it is the minimum LDR that can be observed due to the nonorthogonality of polarizations off of the principal planes. It can also be readily shown that

$$\mathrm{LDR}_V^{(p)} = \mathrm{LDR}_h^{(p)} Z_{dr}^{(p)} \quad (30)$$

$$\mathrm{LDR}_{V,\min} = \mathrm{LDR}_{h,\min} Z_{dr}^{(p)}. \quad (31)$$

III. Experimental Measurements

A. Radar System Description

The phased array used in this study is the first prototype of the "Skyler" radar system [11] developed by Raytheon. Skyler is a low-power, X-band, phased-array radar developed for weather and aviation applications. Earlier publications have referred to this system as the low power radar (LPR) [22]–[24]. The Skyler prototype consists of 2560 dual-polarized antenna elements divided into 20 tiles of 128 elements each. The tiles are based on an integrated, air-cooled, active panel concept [25]. Although the prototype employs liquid cooling, subsequent prototypes are air-cooled.

TABLE I
Skyler Prototype Radar Characteristics

Parameter	Value
Center Frequency	9.6 GHz
Peak/average Power	125 W / 23 W
Bandwidth	<6 MHz
Polarization	Dual H/V (ATAR)
Beamwidth	1.9 Az, 2.1 El
Scan Range	±45 Az, 0-30 El
Range Resolution	60 m
Waveforms	Pulse, NLFM, LFM
Sequences	Single/Dual PRF

Fig. 3. (Left) View of the radiating face of the Skyler Radar prototype with the radome removed. (Right) Photograph of the Skyler Radar installed on the Orchard Hill Tower on UMass Campus.

System characteristics are summarized in Table I, and a photograph of the array face is shown in Fig. 3. The radiating elements are square microstrip patches that are slot-fed. The elements are arranged in an array of 64 × 40 elements (4 × 5 tiles) with a design scan range of 90° in azimuth and 30° in elevation. Each element is controlled by a custom silicon–germanium (SiGe) MMIC chip that includes a power amplifier, low-noise amplifier, transmit/receive and polarization selection switches, programmable attenuator, and phase shifter. As a result, each element has individual amplitude,

$$\mathrm{LDR}_h = \frac{2Re[(\rho_{hx} p_{11}p_{12} + \rho_{vx} p_{21}p_{22} Z_{dr}^{-1/2})(p_{11}p_{22} + p_{12}p_{21})^*]}{\mathrm{LDR}_h^{1/2} |p_{11}p_{22} + p_{12}p_{21}|^2} \quad (28)$$

$$\mathrm{LDR}_{h,\min} = \frac{|p_{11}|^2|p_{12}|^2 + |p_{21}|^2|p_{22}|^2 Z_{dr}^{-1} + 2Re[\rho_{hv} p_{11}p_{12}p_{21}^* p_{22}^*] Z_{dr}^{-1/2}}{|p_{11}|^4 (1 + Z_h)} \quad (29)$$

phase, and polarization control on both transmission and reception.

The array is illuminated with a uniform taper upon transmission and with a 20-dB Taylor distribution upon reception. The peak transmitted power per element is approximately 17 dBm. The SiGe chips in the prototype support one polarization at a time; thus, the polarization scheme employed by the prototype radar is limited to alternate-transmit/alternate-receive (ATAR). Later generations of the MMIC support two simultaneous channels. Because the prototype radar employs the ATAR mode, the copolar correlation coefficient cannot be measured at zero time lag. The method described in [26] is used to estimate its magnitude and phase.

The array is fed by a single analog beamformer through a 2560-channel power divider/combiner. This is achieved via a 1:20 divider feeding each of the 20 tiles comprising the panel. A 128-way divider/combiner is integrated into each of the tiles; thus, each tile has a single RF interconnect. Each tile is further controlled via dedicated power and trigger lines and an ethernet interface over which programming commands are sent to configure and operate the array.

The remainder of the radar consists of an upconverter/downconverter from an intermediate frequency of 60 MHz to the 9.6-GHz center frequency of the array. A software-radio device is used as the digital transceiver for the system. In our case, it is an Ettus Research N210 Universal Software Radio Peripheral (USRP) that has been customized to transmit an arbitrary waveform. Linear and nonlinear FM chirp waveforms are supported with a duty cycle of up to 20%.

Radar operations are achieved by programming the array for a "dwell" consisting of a sequence of pulses along a particular direction. Typically, a dwell consists of two bursts of pulses at two pulse-rates (dual PRF) with polarization diversity incorporated. The most commonly used polarization mode is an alternating H and V polarization, but cross-polarization measurements can also be supported. For each dwell, programming commands are transmitted to each of the tiles that are subsequently executed upon receipt of a common trigger that also controls the software radio.

B. Measurements

In order to determine the projection matrix method described earlier, the system behavior must be accurately characterized. This is done using experimental measurements to obtain the **G** matrix. Many approaches exist for calibrating the amplitude and phase of the beam-peak. It could be measured in a near-field chamber or far-field range, formulated from individual element patterns, or determined in-place from routine measurements.

Here, we consider the latter case in which the radar observes weather targets of opportunity. For this, the radar was installed atop a 20-m tower on the UMass Campus observing a 90° sector to the North. The radar was tilted 15 ° so that the elevation scan range is from 0 ° to 30° in elevation. To collect data for antenna calibration, the radar was operated in a short-range mode so that observations could be obtained at the highest elevation angles while remaining sufficiently below

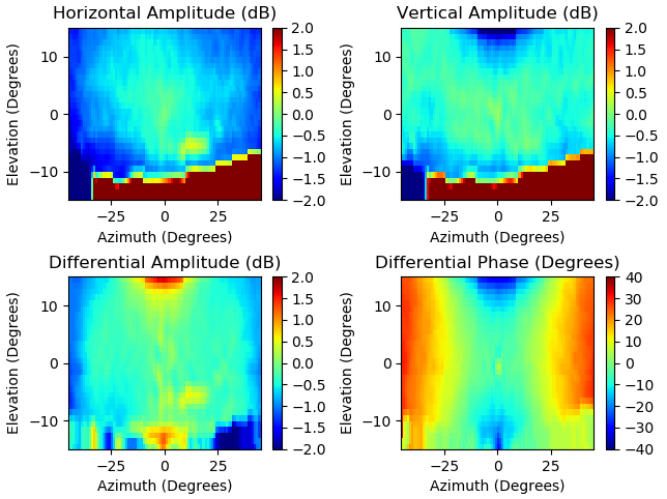

Fig. 4. Measured two-way relative power and relative phase response of Skyler prototype antenna to light rain on September 26, 2019. Power measurements are relative to the horizontal channel at broadside, and the relative phase is taken to be zero at broadside. The lower elevations are corrupted by nearby ground clutter.

the freezing level or overtopping the precipitation. In addition, observations at close range minimize the impact of attenuation and differential propagation phase. Operation at short range necessitates the use of short pulses rather than longer "chirp" waveforms necessary for sensitivity at long range. A 2-μs pulselength was employed. Radar echoes were range corrected by a factor of R^2 and averaged over ranges where SNR exceeded 10 dB for each scan direction. Generally, this corresponds to ranges of less than about 3 km. The averaging was performed over 57 complete scans of the volume, and the average power versus scan angle is shown in Fig. 4. Due to the complex terrain and buildings and trees in the vicinity, the lower few elevation angles were contaminated by ground clutter (much of this through sidelobes). Nonetheless, the average patterns, elsewhere, are fairly uniform, varying by a few dB over the entire scan range.

Due to the symmetry of the antenna construction, we expect that the amplitude and phase patterns are even functions of array-relative azimuth and elevation scan angle. Therefore, in Fig. 5, we replace the contaminated lower elevation angles, with data from the complementary high-elevation angles. Furthermore, we consider the even part of the observations by averaging mirrored versions in azimuth and elevation. We take the differential phase measured at broadside to represent the system (electronics) differential phase, which is removed so that the remaining differential phase is associated with the antenna scan characteristics. Any backscatter differential phase, if present, would be similarly removed. We also apply modest smoothing (averaging over a 5 ° × 5° window). This represents our estimate of the **G** matrix.

Using the measured **G**, the final projection matrix is constructed given that the antenna elements are microstrip patches (magnetic current dipoles implying that the $\mathbf{D}_{\mathbf{m}}$ matrix is used), and the array is tilted to 15 °. The result is shown in Fig. 6. A few observations can be made. First, the element p_{21} is nonzero, and this is due exclusively to the tilt of

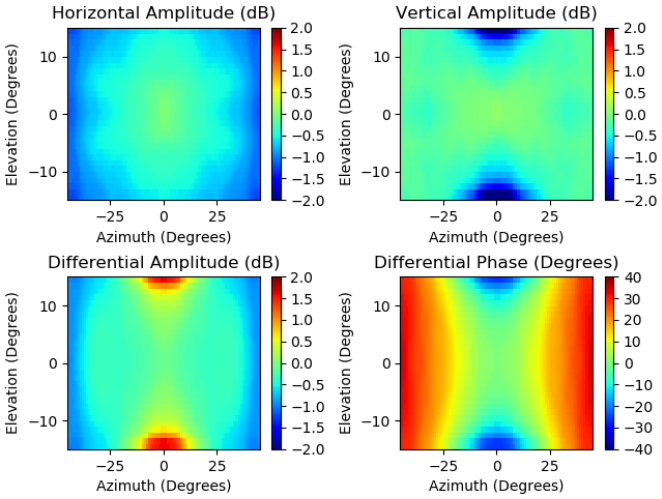

Fig. 5. Even part of two-way relative power and relative phase response of Skyler prototype antenna to light rain with corrupted elevations replaced with complementary high-elevation observations.

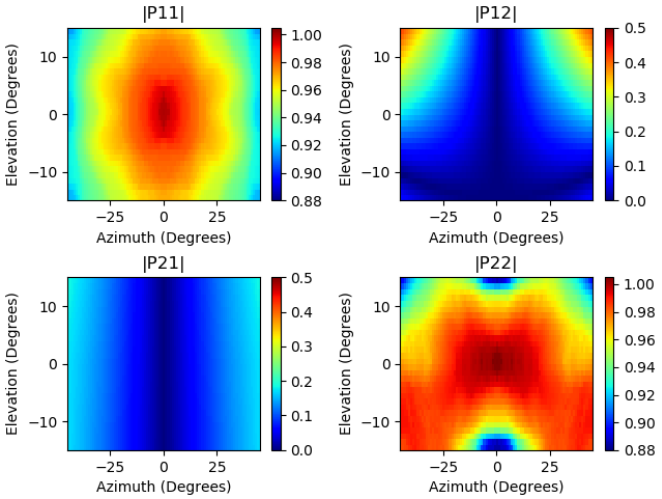

Fig. 6. Magnitude of elements of the final projection matrix **P** with array-relative scan angles for tilt $= 15^\circ$. The scales are in linear units.

the array. For an ideal patch radiator in the vertical plane, p_{21} is identically zero. It is still small compared with the other elements. Second, the elements p_{12} and p_{22} both involve g_{VV}; however, it is not obvious in p_{12}, as the dipole and tilt effects overwhelm the impact of the amplitude pattern.

With the knowledge of **P**, the expected weather product biases can be calculated from the second moments, assuming known intrinsic targets. These are shown in Fig. 7 for the case of a uniform intrinsic reflectivity factor of $Z_h = 30$ dBZ, a differential reflectivity of $Z_{dr} = 1$ dB, a copolar correlation of $\rho_{hv} = 0.9$, and a differential phase of $\varphi_{dp} = 0^\circ$. Also shown is the lower limit of observable linear depolarization ratio, $\mathrm{LDR}_{h,\min}$, which is due principally to the nonorthogonality of the polarizations radiated by the H and V elements.

Also shown in Fig. 7 are contour lines indicating the bounds of acceptable bias for the various weather products. The contour levels are $Z_h^{bias} = -1$ dB, $Z_{dr}^{bias} = \pm 0.2$ dB, $\rho_{hv}^{bias} = 0.01$, and $\varphi_{dp}^{bias} = \pm 3.6^\circ$. The reflectivity and differential reflectivity

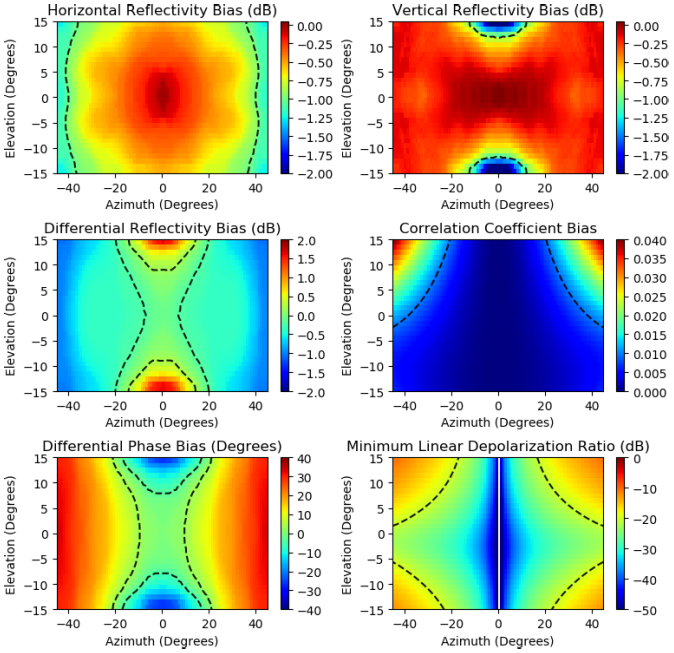

Fig. 7. Weather product biases assuming the projection of Fig. 6 and uniform intrinsic weather variables: $Z_h = 30$ dBz, $Z_{DR} = 1$ dB, $\rho_{hv} = 0.9$, $\varphi_{dp} = 0^\circ$, and Tilt $= 15^\circ$. Dashed contour lines indicate the boundaries between regions of acceptable and unacceptable bias (see text).

bias limits are based on requirements for adequate estimation of rain rate [27]. The correlation coefficient bias requirement may be overly stringent, but the range of this parameter is rather small. The differential phase bias requirement here is based on 1 dB of path-integrated attenuation error assuming $A_{hdB} = 0.28\varphi_{dp}$. (For the WSR-88D radars at S-band, where attenuation is negligible, differential phase accuracy is quoted at 2.5° [28]. The same requirement at X-band, where the wavenumber is about three times greater, would be about 7.5°.) We find that, without correction, reflectivity bias is acceptable over the central portion of the scan range, and the correlation coefficient magnitude is only seriously affected in the upper corners of the scan range. Differential reflectivity and differential phase, however, require correction over most of the scan range.

An "exact" correction of the biased variables can be achieved, in principle, through the use of the inverse of the projection matrix $\mathbf{P}^{-1} = \mathbf{C}$ and by solving for the intrinsic variables as functions of the projected variables. Unlike the forward projection, where intrinsic cross-polarized scattering could be ignored ($s_{hv} = s_{vh} = 0$), the corresponding projected variables cannot be ignored ($s_{hv}^{(p)} = s_{vh}^{(p)} = 0$) due to the nonorthogonality of the projected polarizations. The correction matrix is illustrated in Fig. 8 that shows the magnitudes of the elements with the scan angle. We note that projection inverts cleanly, as it is not far removed from the identity matrix: diagonal elements near unity magnitude and off-diagonal elements small. Still, while it is possible to use the full expressions for correction, it is also desirable to correct observations with minimal calculation so as to minimize further uncertainties introduced by the combinations of measured variables. As pointed out earlier, the p_{21} term is nonzero, but it is small.

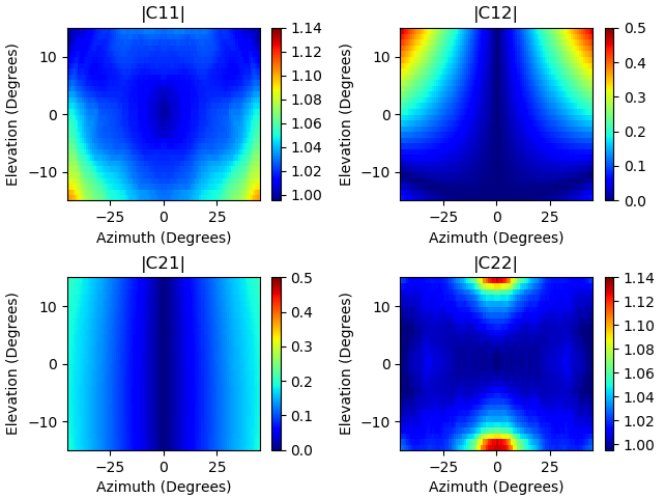

Fig. 8. Same as in Fig. 6 for elements of the correction matrix $\mathbf{C} = \mathbf{P}^{-1}$.

As it appears in equations either squared or raised to the fourth power, it seems reasonable to neglect it. In this case, $Z_h \approx 0$, and the correction for $Z_h^{(p)}$ is simply to divide it by $|p_{11}|^4$. This makes sense since the horizontally polarized fields from the patch elements are well aligned with the $\hat{\varphi}$ direction, which is also only slightly misaligned with $\hat{\varphi}$.

Neglecting p_{21} also simplifies the equation for Z_{dr}; however, given the small dynamic range of Z_{dr} and the precision to which measurements are typically desired, caution is in order. Nonetheless, it is of interest to consider if it may be further simplified. We note that p_{12} is also small for much of the scan range, except in the upper corners of the scan area. Again, however, it appears in the equation for $Z_{dr}^{(p)}$ either raised to the fourth power or squared. If it could be neglected, the correction for $Z_{dr}^{(p)}$ would be to multiply it by $|p_{22}/p_{11}|^4$.

Examining (23) for $\rho_{hv}^{(p)}$, we see the first term multiplying the intrinsic value has an amplitude of exactly unity but captures the projected system differential phase. That is, $\rho_{hv}^{(p)} = |\rho_{hv}^{(p)}| \exp(j\varphi_{dp}^{(p)})$, where $\varphi_{dp}^{(p)}$ is the projected differential phase. The second term adjusts both amplitude and phase. If both p_{21} and p_{12} could be neglected, the expression would include only the first term. Thus, the correction would compensate for the system differential phase only. The results of Fig. 7 indicate that this phase-only correction of $\rho_{hv}^{(p)}$ would be adequate for the lower elevations and central part of the upper elevations but not for the upper corners of the scan range.

The results of the aforementioned partial corrections are shown in Fig. 9, where we find that the partial correction of Z_h is sufficient to achieve 1-dB accuracy over the entire field of view, except for extreme upper corners. Partial correction of Z_{dr} is sufficient to achieve 0.2-dB accuracy over most of the lower elevations, but more precise correction is necessary, particularly in the upper corners of the scan range. A similar result was found by Zrnic *et al.* [13]. With respect to the differential phase, the phase-only correction perfectly compensates it in the case of zero intrinsic differential phase. Fig. 10 shows the same partial correction of polarimetric variables in the case of $\varphi_{dp} = 90^\circ$. This intrinsic differential phase

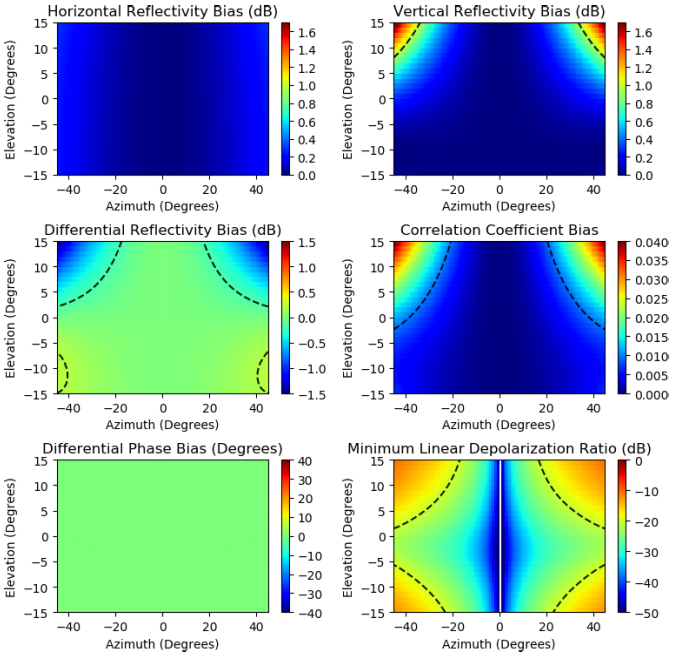

Fig. 9. Same as in Fig. 7 for the case of $\varphi_{dp} = 0^\circ$ with projection-dependent corrections (only) applied.

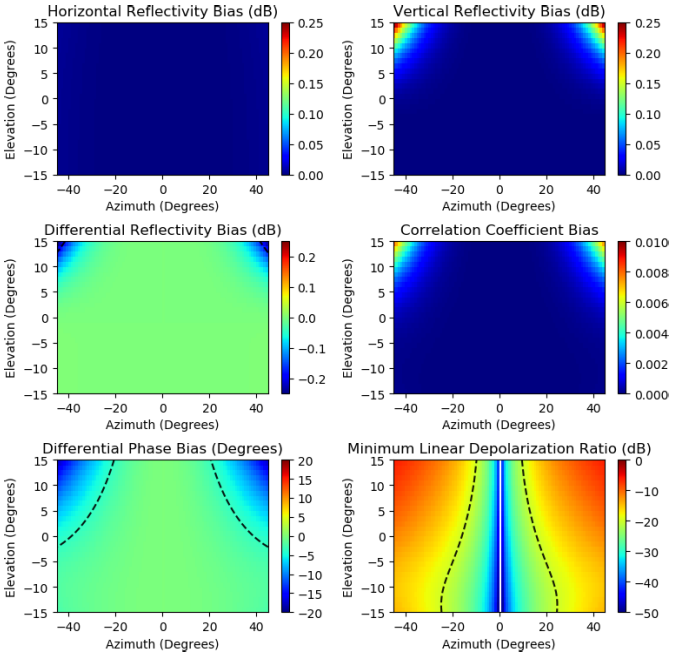

Fig. 10. Same as in Fig. 7 for the case of $\varphi_{dp} = 90^\circ$ with projection-dependent corrections (only) applied.

is consistent with approximately 25 dB of path-integrated attenuation and is representative of the likely maximum value where measurements are possible. We find that the Z_{dr} bias is decreased, but the φ_{dp} bias is increased in the upper corners of the scan range.

Finally, if p_{21} can be neglected, the expression for $\mathrm{LDR}_h^{(p)}$ reduces to

$$\mathrm{LDR}_h^{(p)} \approx \mathrm{LDR}_h \left(\frac{p_{22}}{p_{11}}\right)^2 (1 + \mathrm{LDR}) + \mathrm{LDR}_{h,\min} \quad (32)$$

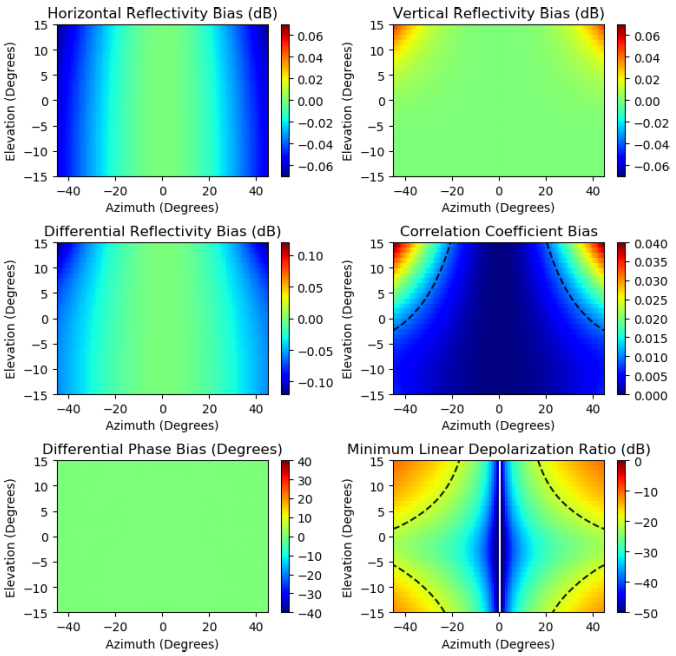

Fig. 11. Same as in Fig. 7 but with $\mathbf{P} = \mathbf{G}$ corrections (only) applied.

$$\mathrm{LDR} \approx \frac{2Re\left[\rho_{hx}\, p_{12} p_{22}^{*}\right]}{\mathrm{LDR}_{h,v}^{1/2}\,|p_{22}|^{2}} \tag{33}$$

$$\mathrm{LDR}_{h,\min} \approx \left(\frac{p_{12}}{p_{11}}\right)^{2}. \tag{34}$$

These expressions reveal that the LDR $_h$ measurement is primarily limited by p_{12}, and that estimates will be biased high even for intrinsic LDR values above the minimum. We show the minimum LDR $_h$ in Fig. 7.

Since we have decomposed the projection into components due to the radar's amplitude and phase properties, antenna properties, and geometry, it is of interest to evaluate the relative impact of the individual components. Fig. 11 illustrates the bias remaining if we compensate only for amplitude and phase (**G**) and ignore projection (**TD**) entirely. Surprisingly, this less-than-partial correction performs better than the partial correction involving the full transformation matrix. It appears that a fortuitous cancellation of error sources is responsible for this result. That is, the error in **P** incurred by ignoring **DT** has the opposite sign to the target-dependent error terms in this case. These compensating errors are associated with the off-diagonal elements of **P**, as the off-diagonal elements of **G** are zero for ideal elements. While it appears to perform better in this case, we cannot claim that this is a general result.

IV. Conclusion

In this article, we have described the projection of radiated polarizations from a PPAR to world-relative coordinates. We have done so in a manner that separates the amplitude and phase characteristics of the radiators from their radiated polarization, enabling the characterization of the radiating elements in their native polarization through observations of simple distributed targets, such as light precipitation. The projection also includes the mechanical tilt (and roll) of the antenna. We have shown how the effect of a wet radome may be incorporated into the amplitude and phase.

This formalism was exercised on an X-band PPAR employing microstrip patch antennas, which was also described. Observations of precipitation were used to obtain the amplitude and phase response of the PPAR, which were combined with the known polarization properties of the antennas and the physical installation (i.e., the tilt). We find that, in general, all elements of the projection matrix are nonzero though one or more of them may be sufficiently small as to be ignored. We have also presented expressions for the polarimetric weather variables (moments) as products of their intrinsic values and projection- and target-dependent corrections. We find that the projection-dependent corrections are sufficient to achieve desired precision over most of the field of view and over the entire field of view for elevation angles below approximately 14 °. At higher elevation angles, target-dependent corrections may become necessary to achieve desired precisions.

Appendix

Wet Radome Effects

Because of its potential impact on measurements, we also consider the possibility of a wet radome covering the face of the PPAR. This is necessary since we use field measurements of precipitation in close proximity to the radar, which implies that the radome is also likely to be wet.

At X-band, a film of water on the radome can yield significant losses [29]. Salazar-Cerreno *et al.* [30] estimated transmission losses for planar radomes, including and lacking hydrophobic coatings. We first consider the latter case, where the water forms a continuous film over the surface rather than beading. This yields the worst case attenuation.

The effect of a wet radome may be considered as a modification to the **G** matrix, where additional attenuation and relative phases are imparted to the radar signal as a function of scan angle due to the water film on the radome. For a flat, rectangular radome tilted from the horizontal, and assuming a uniform, laminar water film, the thickness of the film is found using [30]

$$d_w = \left(\frac{3\mu_k W R}{g \tan\theta_p}\right)^{\frac{1}{3}} \tag{35}$$

where μ_k is the kinematic viscosity of water, W is the width of the square radome, g is gravitational acceleration, R is the rain rate in meters per second, and θ_p is the tilt angle of the radome relative to the horizontal plane. The radome on the Skyler prototype is a thin, coated-fabric, so we consider only the effect of the water film. It imparts a loss given by

$$L = \left|\frac{1 - {}^{2}\, e^{-j\theta_w}}{1 - {}^{2} e^{-j\,2\theta_w}}\right|^{2} \tag{36}$$

where is the air–water reflection coefficient and θ_w is the electrical thickness of the film given by k $_w d_w$, where k_w is the wavenumber in the water. Because the radome is in very close proximity to the radiating elements (a few cm), we use

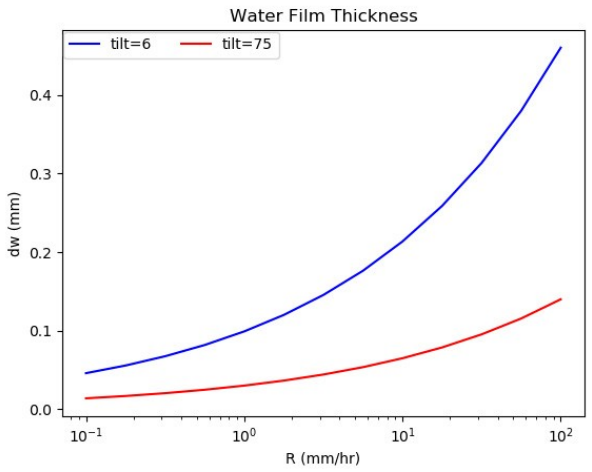

Fig. 12. Radome water film thickness versus rain rate for two array tilt angles.

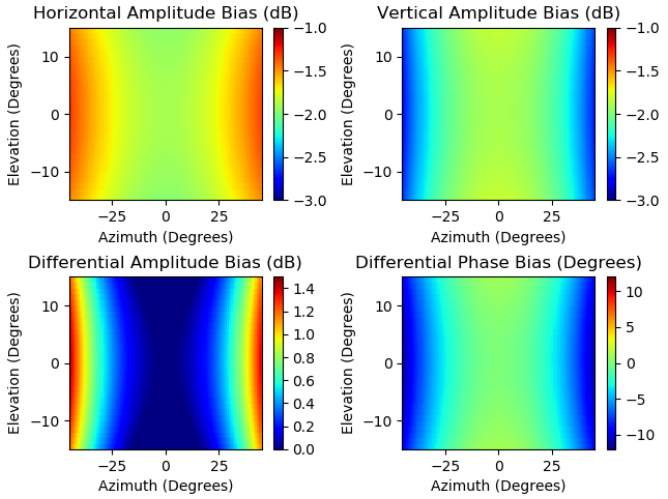

Fig. 13. Impact of water film with scan angle on two-way power and relative phase. Clockwise from upper left H-polarization, V-polarization, differential phase (H-V), and differential power (H/V).

the polarization basis of the elements themselves and consider the effect of the scan angle on the transmission through the wet radome. In general, the plane wave radiated by the array face will impinge on the radome with both parallel (TM) and perpendicular (TE) polarization components relative to the plane of incidence. The plane of incidence is the plane containing the radiation direction $\hat{k}$ and the unit vector normal to the array face $\hat{x}$.

Fig. 12 shows the estimated film thickness from (35) as a function of rain rate for two tilt angles: one corresponding to the typical deployment ($\theta_p = 75^\circ$) and one corresponding to the angle when the array is stowed for transport ($\theta_p = 6^\circ$); in that case, the array points nearly vertically. We observe that the thickness of a water film, in the latter case, is substantially greater than when deployed.

Fig. 13 shows the impact of the water film alone on the H and V polarization channel measurements assuming that $g_{hh} = g_{vv} = 1$. That is, it may be interpreted as the contribution to $\mathbf{G}$ due to the presence of water on the radome. Shown are the two-way transmission losses for H and V polarization, their ratio (indicative of, but not identical to, Z_{dr} bias), and their differential phase. These were calculated assuming a rain rate of 1 mm $\cdot$h^{-1}, a temperature of 17°C, a frequency of 9.6 GHz, and a dielectric constant for pure water of $_w = 60.3 - j\,33.1$ [31]. As can be seen, the impact of a thin film of water on the radome can impart an attenuation exceeding 2 dB and varying by a dB or more with scan angle. This suggests rather substantial attenuation and differential phase as a function of rain rate. However, the assumption of a uniform laminar film tends to overestimate attenuation in many cases [29], [30], so this is a pessimistic estimate of loss.

For radomes with hydrophobic coatings, water will bead on the surface rather than forming a continuous film, and the distribution of drops on the surface will impart substantially less attenuation. Obtaining an accurate expression for the loss requires knowledge of the drop size distribution (DSD) of the rain, properties of the hydrophobic surface, the tilt angle of

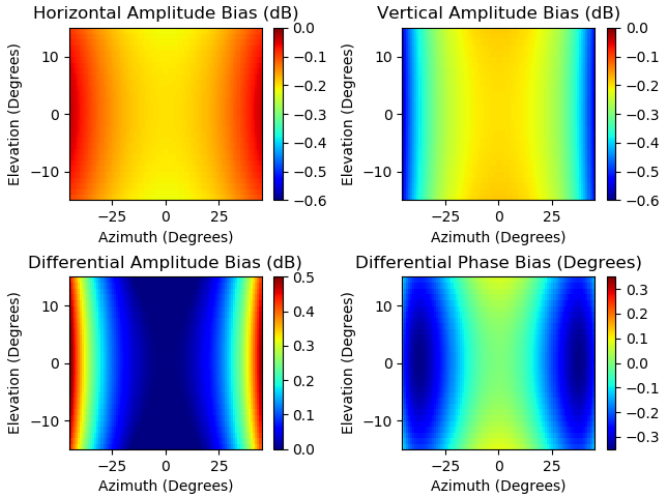

Fig. 14. Impact of water droplets with scan angle on two-way power and relative phase. Clockwise from upper left H-polarization, V-polarization, differential phase (H-V), and differential power (H/V).

the radome, and the rain duration. Salazar-Cerreño *et al.* [30] and Mancini *et al.* [32] showed the measured and modeled attenuations at X-band and S-band, respectively. To speed calculation, they employed a mixing model to arrive at an effective dielectric constant for the layer of droplets covering the radome, where the key parameter was the overall fraction of the droplet-layer volume consisting of water. The effective dielectric constant of the droplet layer was given by the Maxwell–Garnett equation

$$_{\text{eff}} = \frac{2\delta(_r - 1) + _r + 2}{2 + _r - \delta(_r - 1)} \tag{37}$$

where $_r$ is the relative permittivity of water, and δ is the fractional volume of water contained in the droplet layer. The droplet layer thickness was determined by the maximum droplet size in the DSD and surface properties (drops exceeding a given size will roll off). While this fraction

will vary with rain rate, DSD, rain duration, and surface properties, numerical simulations for a coated fabric tilted 15° from the vertical, as used by the Skyler prototype, show that it is generally a small fraction of the order of 10%. The resulting attenuation assuming a volume fraction of 10% and a droplet layer thickness of 5 mm on a Teflon material is shown in Fig. 14. In this case, the attenuation is only a fraction of a decibel though still significant enough to compromise differential reflectivity measurements near the scan edges if uncompensated. Although the layer thickness is much greater than the continuous film case, the effective dielectric constant is much lower than that of pure water. We do note that, for the Maxwell–Garnett relation to be valid, it is necessary that the droplet size has to be a small fraction of the wavelength in the effective medium ($d \ll \lambda_{\text{eff}}/10$) [33]. While this size criterion is satisfied for most droplets at X-band, it is not satisfied with the largest droplets. This result is more representative of the loss properties of the Skyler prototype radome under wetting. Nonetheless, the field measurements of **G** may be assumed to be influenced by the presence of water on the radome.

ACKNOWLEDGMENT

The authors gratefully acknowledge the assistance of Casey Wolsieffer, Max Adam, and Jezabel Vilardell-Sanchez in the deployment of the Skyler prototype. They would like to thank Michael Dubois, Eric Knapp, Chris McCarroll, and Richard Moro of Raytheon for facilitating the loan of the Skyler prototype and providing the technical assistance necessary for its use in research. They would also like to thank the anonymous reviewers for their insightful comments.

REFERENCES

[1] D. S. Zrnić *et al.*, "Agile-beam phased array radar for weather observations," *Bull. Amer. Meteorol. Soc.*, vol. 88, no. 11, pp. 1753–1766, 2007.

[2] P. L. Heinselman, D. L. Priegnitz, K. L. Manross, T. M. Smith, and R. W. Adams, "Rapid sampling of severe storms by the national weather radar testbed phased array radar," *Weather Forecasting*, vol. 23, no. 5, pp. 808–824, Oct. 2008.

[3] S. M. Torres and K. Hondl, "The advanced technology demonstrator at the national severe storms laboratory," in *Proc. 10th Eur. Conf. Radar Meteorol. Hydrol. (ERAD)*, 2018, p. 178.

[4] S. M. Torres *et al.*, "An update on the advanced technology demonstrator at the national severe storms laboratory," in *Proc. 36th Conf. Environ. Informat. Proc. Technol., AMS Annu. Meeting*, Boston, MA, USA, Jan. 2020, Paper 8B.1.

[5] J. Wurman and M. Randall, "An inexpensive, mobile, rapid-scan radar," in *Proc. 30th Int. Conf. Radar Meteorol.*, Munich, Germany, 2001, pp. 3–4.

[6] H. B. Bluestein, M. M. French, I. Popstefanija, R. T. Bluth, and J. B. Knorr, "A mobile, phased-array Doppler radar for the study of severe convective storms: The MWR-05XP," *Bull. Amer. Meteorol. Soc.*, vol. 91, no. 5, pp. 579–600, 2010.

[7] B. Isom *et al.*, "The atmospheric imaging radar (AIR) for high-resolution observations of severe weather," in *Proc. IEEE RadarCon (RADAR)*, Kansas City, MO, USA, May 2011, pp. 627–632.

[8] J. L. Salazar, R. Medina, E. J. Knapp, and D. J. McLaughlin, "Phase-tilt array antenna design for dense distributed radar networks for weather sensing," in *Proc. IEEE Int. Geosci. Remote Sens. Symp. (IGARSS)*, Boston, MA, USA, Jul. 2008, p. V-318.

[9] A. Hopf *et al.*, "CASA phased array radar system description, simulation and products," in *Proc. IEEE Int. Geosci. Remote Sens. Symp. (IGARSS)*, Cape Town, South Africa, Jul. 2009, pp. 1–4.

[10] K. Orzel, L. Masiunas, T. Hartley, and S. Frasier, "Deployment of an X-band dual-polarization phased array radar in the Dallas-Fort Worth urban demonstration network," in *Proc. 8th Eur. Conf. Radar Meteorol. Hydrol. (ERAD)*, Garmisch-Partenkirchen, Germany, Sep. 2014, pp. 1–5.

[11] Raytheon. (2019). *Skyler*. Accessed: Dec. 5, 2019. [Online]. Available: https://www.raytheon.com/capabilities/products/skyler

[12] G. Zhang, R. J. Doviak, D. S. Zrnic, J. Crain, D. Staiman, and Y. Al-Rashid, "Phased array radar polarimetry for weather sensing: A theoretical formulation for bias corrections," *IEEE Trans. Geosci. Remote Sens.*, vol. 47, no. 11, pp. 3679–3689, Nov. 2009.

[13] D. S. Zrnic, G. Zhang, and R. J. Doviak, "Bias correction and Doppler measurement for polarimetric phased-array radar," *IEEE Trans. Geosci. Remote Sens.*, vol. 49, no. 2, pp. 843–853, Feb. 2011.

[14] R. J. Doviak, L. Lei, G. Zhang, J. Meier, and C. Curtis, "Comparing theory and measurements of cross-polar fields of a phased-array weather radar," *IEEE Geosci. Remote Sens. Lett.*, vol. 8, no. 5, pp. 1002–1006, Sep. 2011.

[15] L. Lei, G. Zhang, and R. J. Doviak, "Bias correction for polarimetric phased-array radar with idealized aperture and patch antenna elements," *IEEE Trans. Geosci. Remote Sens.*, vol. 51, no. 1, pp. 473–486, Jan. 2013.

[16] L. Lei, G. Zhang, R. J. Doviak, and S. Karimkashi, "Comparison of theoretical biases in estimating polarimetric properties of precipitation with weather radar using parabolic reflector, or planar and cylindrical arrays," *IEEE Trans. Geosci. Remote Sens.*, vol. 53, no. 8, pp. 4313–4327, Aug. 2015.

[17] C. Pang *et al.*, "Polarimetric bias correction of practical planar scanned antennas for meteorological applications," *IEEE Trans. Geosci. Remote Sens.*, vol. 54, no. 3, pp. 1488–1504, Mar. 2016.

[18] K. Orzel and S. J. Frasier, "Weather observation by an electronically scanned dual-polarization phase-tilt radar," *IEEE Trans. Geosci. Remote Sens.*, vol. 56, no. 5, pp. 2722–2734, May 2018.

[19] Z. Li *et al.*, "Polarimetric phased array weather radar data quality evaluation through combined analysis, simulation, and measurements," *IEEE Geosci. Remote Sens. Lett.*, early access, May 14, 2020, doi: 10.1109/LGRS.2020.2990334.

[20] N. A. Aboserwal, J. L. Salazar, J. A. Ortiz, J. D. Diaz, C. Fulton, and R. D. Palmer, "Source current polarization impact on the cross-polarization definition of practical antenna elements: Theory and applications," *IEEE Trans. Antennas Propag.*, vol. 66, no. 9, pp. 4391–4406, Sep. 2018.

[21] A. Ludwig, "The definition of cross polarization," *IEEE Trans. Antennas Propag.*, vol. 21, no. 1, pp. 116–119, Jan. 1973.

[22] P. Drake, J. Bourgeois, and D. McLaughlin, "X-band phased array radar: Current radar performance and plans for wake vortex experimentation," in *Proc. WakeNet-Eur. Workshop*, Bretigny, France, May 2014, pp. 13–14.

[23] D. L. Pepyne *et al.*, "Raytheon X-band polarimetric phased-array radar: Weather data processing first look," in *Proc. 31st Conf. Environ. Inf. Process. Technol.*, Phoenix, AZ, USA, Jan. 2015, p. 923.

[24] A. P. Hopf, J. Bourgeois, P. R. Drake, and T. J. Flynn, "Raytheon polarimetric X-band phased-array radar: Single and netted radar system," in *Proc. 31st Conf. Environ. Inf. Process. Technol.*, Phoenix, AZ, USA, Jan. 2015, p. 7A.1A.

[25] A. Puzella and R. Alm, "Air-cooled, active transmit/receive panel array," in *Proc. IEEE Radar Conf.*, Rome, Italy, May 2008, pp. 26–30.

[26] M. Sachidananda and D. S. Zrnić, "Efficient processing of alternately polarized radar signals," *J. Atmos. Ocean. Technol.*, vol. 6, no. 1, pp. 173–181, 1989.

[27] Y. Wang and V. Chandrasekar, "Polarization isolation requirements for linear dual-polarization weather radar in simultaneous transmission mode of operation," *IEEE Trans. Geosci. Remote Sens.*, vol. 44, no. 8, pp. 2019–2028, Aug. 2006.

[28] C. A. Stephenson, *Interface Control Document for the RDA/RPG, RDA Build 18.0*, Document Number 2620002R, WSR-88DRadar Operations Center, Norman, OK, USA, 2018.

[29] S. J. Frasier *et al.*, "In-place estimation of wet radome attenuation at X-band," *J. Atmos. Ocean. Technol.*, vol. 30, no. 5, pp. 917–928, 2013.

[30] J. L. Salazar-Cerreño *et al.*, "A drop size distribution (DSD)-based model for evaluating the performance of wet radomes for dual-polarized radars," *J. Atmos. Ocean. Technol.*, vol. 31, no. 11, pp. 2409–2430, 2014.

[31] T. Meissner and F. J. Wentz, "The complex dielectric constant of pure and sea water from microwave satellite observations," *IEEE Trans. Geosci. Remote Sens.*, vol. 42, no. 9, pp. 1836–1849, Sep. 2004, doi: 10.1109/TGRS.2004.831888.

[32] A. Mancini, R. M. Lebrón, and J. L. Salazar, "The impact of a wet *S*-band radome on dual-polarized phased-array radar system performance," *IEEE Trans. Antennas Propag.*, vol. 67, no. 1, pp. 207–220, Jan. 2019.

[33] A. H. Sihvola, "Mixing rules with complex dielectric coefficients," *Subsurf. Sens. Technol. Appl.*, vol. 1, no. 4, pp. 393–415, 2000.

William Heberling (Student Member, IEEE) received the B.S. degree in electrical engineering from the New Jersey Institute of Technology, Newark, NJ, USA, in 2015. He is pursuing the Ph.D. degree in electrical engineering with the University of Massachusetts at Amherst, Amherst, MA, USA.

He is a Graduate Research Assistant with Microwave Remote Sensing Laboratory, University of Massachusetts at Amherst. His research interests include weather radar design and phased-array antenna technology.

Stephen J. Frasier (Senior Member, IEEE) received the B.E.E. degree from the University of Delaware, Newark, DE, USA, in 1987, and the Ph.D. degree from the University of Massachusetts at Amherst, Amherst, MA, USA, in 1994.

From 1987 to 1990, he was with SciTec, Inc., Princeton, NJ, USA, analyzing the electromagnetic and optical signatures of rocket plumes, evaluating laser detection systems, and developing data acquisition systems supporting airborne IR sensors. In 1990, he joined Microwave Remote Sensing Laboratory, University of Massachusetts at Amherst, where his graduate work involved the development and use of digital-beamforming phased-array radar for oceanographic research applications. In 1997, he joined the faculty at the University of Massachusetts at Amherst, where he is a Professor and Co-Director of the Microwave Remote Sensing Laboratory. From 2005 to 2006, he spent a sabbatical year with the Polytechnic University of Catalonia, Barcelona, Spain, studying LiDAR techniques for atmospheric profiling, and in 2012, he spent a sabbatical year with Météo-France, Toulouse, France, evaluating the performance of an X-band weather radar network being deployed in the Maritime Alps. He has coauthored over 50 refereed journal publications. He leads radar research programs studying ocean surface winds, advanced radar methods for profiling the atmospheric boundary layer, and application of phased-array technology to meteorological radar polarimetry. His research interests include microwave imaging and interferometric techniques, radar oceanography, and radar meteorology.

Dr. Frasier is also a Senior Member of the IEEE Geoscience and Remote Sensing Society and a member of the URSI Commission F and the American Meteorological Society. From 2015 to 2018, he served as the Co-Chair of the Airborne Phased-Array Radar Advisory Panel to the National Center for Atmospheric Research. He has served as an Associate Editor for the journal *Radio Science* from 2003 to 2010. He has been an Associate Editor for the IEEE TRANSACTIONS ON GEOSCIENCE AND REMOTE SENSING since 2010.